

1 A frequency-approximated approach to Kirchhoff migration

2 Mark E. Vardy* and Timothy J. Henstock*

3 *School of Ocean and Earth Science,

4 University of Southampton

5 National Oceanography Centre, Southampton

6 European Way, Southampton

7 UK

8 SO14 3ZH

9 Email: mev@noc.soton.ac.uk and then@noc.soton.ac.uk

10 (January 5, 2011)

11 GEO-2009-0386.r2

12 Running head: Frequency-Approximated Kirchhoff Migration

ABSTRACT

13 The integral solution of the wave equation has long been one of the most popular methods
14 for the imaging (Kirchhoff migration) and inversion (Kirchhoff inversion) of seismic data.
15 For efficiency, this process is commonly formulated as a time-domain operation on each
16 trace, applying antialiasing through high-cut filtering of the operator or pre-/postmigration
17 dip filtering. Migration in the time domain, however, does not allow for velocity dispersion,
18 while standard antialiasing methods assume a flat reflector and tend to over-filter the data.
19 This paper recasts the Kirchhoff integral in the frequency domain, enabling robust antialias
20 filtering through appropriate dip limiting of each frequency and implicit accommodation of
21 true dispersion. It is shown that full frequency decomposition of the input seismogram can

22 be approximated by band-pass filtering (or correlation with band-limited source sweeps for
23 Chirp/Vibroseis data) into few narrow-band traces that cumulatively retain the full source
24 bandwidth. From prior knowledge of the source waveform we define suitable bandwidths to
25 describe broadband (3.0 octaves) data using just six frequency bands. Kirchhoff migration
26 of these narrow-band traces using coefficients determined at their central frequencies is
27 shown (using synthetic and field data) to significantly improve the preservation of higher
28 frequencies and cancellation of steeply dipping aliased energy over traditional time domain
29 antialiasing methods. If, however, two bands per octave ceases to be a robust approach,
30 this frequency-approximated approach provides the processor with ultimate control over the
31 frequency decimation, allowing increased resolution afforded by more bands to be balanced
32 against the computational cost, while the number of frequency bands are few enough to
33 permit detailed control over frequency dependent antialias filtering parameters.

INTRODUCTION

34 The geometrical approach to migration described by Hagedoorn (1954) is an elegantly sim-
35 ple and effective technique. Expanded into a mathematical treatment of diffraction response
36 using Kirchhoff's retardation potential solution to the wave equation (Troyer, 1970; Hilter-
37 man, 1970, 1975; Berryhill, 1977), it has been used extensively for both prestack imaging
38 (Schneider, 1978) and inversion (e.g., Bleistein, 1987; Docherty, 1991; Gray, 1997). Since
39 data are considered trace-by-trace, it has proven to produce reliable images when spatial
40 sampling is irregular, theoretically can move energy to any dip angle, and (during migra-
41 tion) is robust in low signal-to-noise (S/N) environments by mixing energy from different
42 traces and times.

43 This paper concentrates on Kirchhoff migration, which can be thought of as a math-
44 ematical treatment of Hagedoorn's 'string construction technique' using Green's theorem
45 (Bleistein, 1999; Bleistein and Gray, 2001). Sample-by-sample contributions from the input
46 seismogram are summed over an equal travelttime curve, using the constructive summation
47 of 'real' events and destructive cancellation of 'noise' to produce a geometrically correct mi-
48 grated image. Correct weighting of the contributions from each of these samples can result
49 in a true-amplitude volume (Hubral et al., 1991; Docherty, 1991; Gray, 1997; Schleicher
50 et al., 2007). This approach to imaging readily accommodates vertical velocity gradients
51 and gentle horizontal velocity gradients, but struggles with sharp, steeply dipping velocity
52 variations where the Green's function becomes multi-valued and the summation surface
53 multi-branched (Hubral, 1977). Recent increases in commonly available computing power
54 have encouraged the growth of wavefield continuation methods (such as reverse-time or
55 downward-continuation migration; Baysal et al., 1983; Whitmore, 1983), which are more

56 robust in areas of discrete velocity contrasts. However, the efficiency and availability of
57 Kirchhoff codes, as well as their robustness to irregular spatial sampling, has ensured their
58 continued popularity.

59 While efficient compared to wavefield-continuation migration, optimal Kirchhoff imaging
60 of modern seismic reflection data (which is decimated in both time and space, making it
61 prone to aliasing of higher frequencies) can still be computationally expensive, especially
62 when trying to migrate broad bandwidth data. This arises from the desire to perform
63 migration in the frequency domain, where the input seismogram is frequency decomposed
64 in order to use a frequency-dependant operator for antialias filtering and to accommodate
65 dispersion. A theoretically exact approach to frequency-decomposition, such as the short-
66 time Fourier transform (STFT), leads to oversampling in the frequency domain relative
67 to the sensitivity of the final image, multiplying the number of input traces by several
68 thousand. For this reason, most modern Kirchhoff migration algorithms operate in the
69 time domain, antialiasing through: interpolation to smaller trace spacing (Bardan, 1987;
70 Yilmaz, 1987); dip filtering pre- or postmigration in either the f - k or τ - p domain (e.g.,
71 Biondi, 2001); or operator weighting using a filter-bank (e.g., Bevc and Claerbout, 1992;
72 Claerbout, 1992; Gray, 1992; Lumley et al., 1994). Although effective, these approaches do
73 not allow for true velocity dispersion, attenuation compensation (which may be particularly
74 significant with high-resolution data; Buckingham, 2000), tend to over-filter data (Abma
75 et al., 1998), and can be expensive (involving inversion or two multi-dimensional Fourier
76 transforms).

77 We return to the frequency domain, correcting the oversampling by modifying an opti-
78 mization approach that is commonly used for inversion algorithms by inverting for localized
79 frequencies (e.g., Pratt and Worthington, 1988; Lauo and McMechan, 1996; Forgues et al.,

80 1998; Sirgue and Pratt, 2004). These inversion methods, however, do not preserve the full
81 bandwidth of the original data for limited offsets (Freudenreich and Singh, 2000). This
82 makes them ill-suited to migration, where preserving the full bandwidth is important for
83 noise cancellation and to optimize resolution. Instead, we approximate the frequency de-
84 composition by band-pass filtering into a small number of narrow band traces, which are
85 Kirchhoff migrated using coefficients determined at their central frequencies. In this man-
86 ner, the full bandwidth is preserved and imaging can be optimized at each frequency band to
87 prevent aliasing and account for dispersion, while limiting the decrease in efficiency between
88 time and frequency domain applications through a reduction in the number of frequency-
89 decomposed traces to be migrated. Using synthetic and field data examples, we show that
90 high fidelity images can be produced using few bands (6 for this application) defined using
91 prior knowledge of the source bandwidth. Higher frequencies are better preserved than in
92 common, time domain antialiased imaging, and independent treatment of the frequency
93 content affords more effective noise cancellation. This is obtained with only a modest in-
94 crease in run times (factor of 2) over the most simple dip-limited time-domain Kirchhoff
95 migration.

MATHEMATICAL CONSTRUCT

96 Conceptually, Kirchhoff migration involves the summation of energy over equal traveltime
97 curves, which is mathematically described by the integral solution of the (inhomogeneous)
98 wave equation. A brief outline of the basic mathematics follows, and the reader is referred
99 to standard texts for a more complete derivation (e.g., Bleistein, 2001).

100 **Kirchhoff imaging**

101 The full mathematical approach takes the form of a surface integral over the wavefront in
102 the half-space of $z > 0$ using Green's Theorem, known as the Kirchhoff integral (Schneider,
103 1978):

$$p(r, t) = \frac{1}{2\pi} \int_{t_0} \int_A p(r_0, t_0) \frac{\partial}{\partial z_0} \left[\frac{\delta(t - t_0 - \frac{R}{v})}{R} \right] dA dt_0, \quad (1)$$

104 where $p(r, t)$ is the wavefront at location r and traveltime t , A is the migration aperture,
105 $p(r_0, t_0)$ is the wavefront at source location r_0 and time t_0 , $\delta(t - t_0 - \frac{R}{v})$ is the appropriate
106 Dirac delta function, where v is the velocity, and R is a vector connecting the source and
107 observation locations, i.e., r_0 and r , respectively. Equation 1 is equivalent to expressing
108 the migration process performed over aperture A , as a 3D, frequency-domain convolution
109 between the recorded wavefield and a space-time operator (Schneider, 1978). It can be
110 recast in terms of a downward-continued wavefield (Claerbout and Doherty, 1972), giving
111 the downward-continued Kirchhoff integral:

$$p(x, y, z, t = 0) = \int_A -\frac{1}{2\pi R} \frac{\partial}{\partial z} p(x, y, z = 0, t = 2R/v) dA, \quad (2)$$

112 where $p(x, y, z = 0, t = 2R/v)$ is the wavefront as observed in a upgoing reference frame
113 traveling at velocity $v/2$ (half the subsurface velocity). Equation 2 defines the simplest
114 form of Kirchhoff migration, where each trace is differentiated and energy spread across
115 equal travelttime curves in the time domain. However, performing migration in the time
116 domain does not allow for velocity dispersion (resulting in the loss of higher frequencies),
117 and imposes the aliasing limits of the highest frequency on all others (thereby limiting the

118 maximum dip angle that can be coherently imaged).

119 Although there is no method for accommodating dispersion completely, a number of
120 different approaches have been proposed that afford better control over the frequency de-
121 pendence of the Kirchhoff operator, while still preserving migration as a time-domain oper-
122 ation. These can be thought of as three basic types of antialias filter: interpolation methods
123 that operate premigration; truncation of the Kirchhoff operator; and dip filtering pre- or
124 postmigration. Interpolating the input data to a finer spatial sampling in the acquisition
125 or offset domain is the traditional approach (Bardan, 1987; Yilmaz, 1987), but this can be
126 time consuming and inaccurate (especially for data sets containing steep dips). A more
127 robust approach approximates a true frequency-domain antialias filter as a set of spatially-
128 varying low-pass filters that produce an offset-varying high-cut filtered Kirchhoff operator
129 (Bevc and Claerbout, 1992; Claerbout, 1992; Gray, 1992; Lumley et al., 1994). These fil-
130 ters, although effective at removing aliased energy, commonly over-filter the data leading to
131 lower resolution images than otherwise might be possible (particularly when reflectors are
132 not horizontal; Biondi, 2001) and can be computationally expensive. Frequency-dependent
133 dip-filtering can be readily applied in either the f - k or τ - p domain (e.g., Biondi, 2001;
134 Lokshtanov et al., 2002). However, this comes at the computational cost of applying two
135 multidimensional Fourier transforms (which can be expensive) with associated data preser-
136 vation issues for finite data sets. Alternatively, an accurate solution can be obtained by
137 recasting equation 2 in the frequency domain. This allows true velocity dispersion to be
138 explicitly accommodated and the balance between imaging and antialias filtering optimized
139 through the migration of each frequency component to an appropriate maximum dip.

140 Basic Fourier theory tells us that $\frac{\partial}{\partial t} f(t) \leftrightarrow i\omega F(\omega)$. Hence, by considering the observed
141 wavefield as the superposition of infinitely many monochromatic wavefields, the kernel of

142 equation 2 (the downward-continued Kirchhoff integral) becomes:

$$\frac{\partial}{\partial z} p(x, y, z = 0, t = 2R/v) = \frac{1}{v} \int_{\omega} i\omega P(x, y, z = 0, \omega) e^{-i\omega t} d\omega, \quad (3)$$

143 where $P(x, y, z = 0, \omega)$ is a frequency-decomposed version of the recorded trace.

144 This leads to a frequency-domain expression for 3D Kirchhoff imaging (Bleistein and
145 Gray, 2001):

$$I(\xi) = \int_A W(x, y, z, t) \int_{\omega} i\omega P(x, y, z, \omega) e^{-i\omega t} d\omega dA. \quad (4)$$

146 $W(x, y, z, t)$ is a weighting function that combines $1/v$ with terms to account for the
147 obliquity, the angular dependence of amplitudes generated by a Huygens' secondary source,
148 and spherical spreading. In practice, because the recorded wavefield is quantized, we use
149 multi-dimensional summation rather than a pure integration, and introduce a frequency-
150 dependent weight function, $D(\omega)$, to prevent aliasing of higher frequencies (effectively fre-
151 quency dependent limiting of the maximum dip angle).

152 Frequency-approximated Approach

153 Although solving the Kirchhoff integral in the frequency domain allows dispersion and
154 operator frequency dependence to be readily accommodated, treating the Kirchhoff integral
155 as the sum over frequency decomposed traces significantly increases the number of traces
156 to be migrated. For broad bandwidth sources, such as the Chirp data example we use
157 later (3.0 octaves; 1.5 – 13.0 kHz; Gutowski et al., 2002), the theoretically exact frequency
158 decomposition by STFT multiplies the number of traces by a factor of several thousand.

159 If, instead, the data are transformed into a series of narrow-band traces through band-
 160 pass filtering or correlation with a series of band-limited sweeps (for swept frequency sources
 161 such as Chirp or Vibroseis), these data can then be migrated according to:

$$I(\xi) = \sum_A W(x, y, z, t) \sum_{\omega=1}^{N_\omega} D(\omega) i\omega_c p_\omega(x, y, z, t), \quad (5)$$

162 where p_ω is the band-limited trace, N_ω is the number of frequency bands used, and
 163 ω_c the central frequency for each band. The validity of equation 5 is dependent upon the
 164 frequency bands being narrow enough for ω_c to be representative of the band as a whole.
 165 As discussed later, suitable bands can be readily derived from knowledge of the source
 166 waveform, allowing the full source bandwidth to be represented by only a few (e.g., six)
 167 decomposed traces.

168 Since the data are not Fourier-transformed, the multiplication by $i\omega_c$ has to be ap-
 169 proximated. This can be done as a straight -90-degree phase shift based on the central
 170 frequency, ω_c , using interpolation to accommodate $\lambda/4v \neq \Delta t$. Similarly, taking the Hilbert
 171 transform post-correlation will also approximate the phase shift. For monochromatic traces,
 172 the Hilbert transform is exactly equivalent to a 90-degree phase shift (since, if $f(t) = \sin(t)$,
 173 $H(f(t)) = -\cos(t)$), but for finite-bandwidth signals this relationship no longer holds ex-
 174 actly.

175 Alternatively, a theoretically exact solution can be obtained through the differentia-
 176 tion of each band-limited trace (similar to equation 2), equation 5 becoming a practical
 177 expression for frequency-approximated Kirchhoff imaging:

$$I(\xi) = \sum_A W(x, y, z, t) \sum_{\omega=1}^{N_\omega} D(\omega) \frac{\partial}{\partial t} p_\omega(x, y, z, t). \quad (6)$$

178 In this manner, the frequency-domain sampling can be controlled to levels more suitable
 179 to the frequency sensitivity of the final image, while simultaneously preserving the full source
 180 bandwidth.

EXAMPLE RESULTS

181 To illustrate the effect of Kirchhoff migrating a limited number of narrow-band traces,
 182 we consider two example data sets migrated using the frequency-approximated Kirchhoff
 183 migration and a standard time-domain prestack antialiased Kirchhoff migration using the
 184 frequency-selective operator of Gray (1992) implemented using Landmark's ProMAX soft-
 185 ware. First we image a synthetic volume generated using the Phase Screen forward mod-
 186 eling approach of Wild and Hudson (1998), and secondly a small (30×30 m) subset of a
 187 high-resolution data set acquired in an atidal basin on the south coast of the UK (Vardy
 188 et al., 2008). Both are prestack time-migrated using a constant velocity model of 1500 m/s,
 189 allowing additional optimizations for this kind of near-surface application.

190 **Synthetic Example**

191 A stepped reflector with a sinusoidal morphology (Figure 1) was forward modelled using the
 192 Phase Screen 3D forward modelling code (Wild and Hudson, 1998). The model is decimated
 193 into a series of elastic screens, and the upgoing and downgoing wavefields propagated as
 194 plane waves between them. The receiver array and source function were designed to mimic
 195 acquisition of 3D Chirp subbottom profiler data (Bull et al., 2005), with an inline and

196 crossline hydrophone spacing of 0.25 m and source frequency content of 1.5 – 13.0 kHz. A
197 small asymmetry was introduced into the surface steps such that steps to the left of a peak
198 were 5.0 cm higher than on the right (Figure 1c). This, together with the sharp reflector
199 terminations, poses a stringent test of the migration performance since such a difference is
200 resolvable with the source bandwidth (peak-to-side lobe distance is ± 2.9 cm for a 1.5 – 13.0
201 kHz source).

202 Figure 2 shows vertical sections and time slices through the imaged volume migrated
203 using the ProMAX algorithm, a) and c), and the frequency-approximated method, b) and
204 d), using the six bands defined in Table 1. In both cases, anomalous reflectors are found
205 in the peaks and troughs of the sinusoid caused by decimation of the wavefield into a
206 series of elastic screens (red arrows, Figure 2). Similarly, horizontal energy leakage smears
207 reflectors laterally due to limitations in the plane-wave assumption (blue arrows, Figure
208 2). In addition, the spatial sample interval of 0.125 m limits dip angles such that only
209 reflections from the horizontal parts of the stepped interface are imaged. However, these
210 anomalies are consistent between the two imaged volumes, which are highly comparable.

211 Vertical sections in Figures 2a and 2b show very similar reflector reconstruction. There
212 is a clear increase in vertical resolution gained by performing the migration in the frequency-
213 domain, affording significantly improved imaging of the asymmetry between reflectors either
214 side of the peaks (Figures 2d and 2e). This is apparent in the time slices (extracted at 13.78
215 ms twt; Figures 2f and 2g), which show a clear distinction between reflectors to the left and
216 right of the peak in the frequency-approximated volume. Traces extracted 1.0 m into each
217 section (Figure 2c) show only minor differences in wavelet reconstruction for the standard
218 (gray) and frequency-approximated (black) algorithms.

219 Figure 3 shows the results of a sensitivity test using the same synthetic volume. Random
220 noise was introduced into the data pre-migration using the ProMAX Additive Noise and
221 Spike tool. Noise levels were varied such that the peak amplitude S/N decreased from
222 $S/N = 5$ to $S/N = 1$ (Figures 3c through 3h). Images generated using both migration
223 schemes show the expected increased contamination by uncancelled, steeply-dipping energy
224 with decreasing S/N , but is constrained better in the frequency-approximated Kirchhoff-
225 migrated profiles (black boxes, Figures 3g and 3h).

226 **Field data example**

227 Migrating synthetic data volumes (Figures 2 and 3) demonstrates, in principle, that per-
228 forming prestack Kirchhoff migration in the frequency domain using the frequency-approximated
229 approach enhances vertical resolution and affords better control over the removal of aliased
230 energy. It is, however, also necessary to investigate performance in the presence of noise
231 (both truly random and systematic) and irregular sampling using field data. Therefore, we
232 image a subset of a data volume acquired in a man-made atidal harbour basin on the south
233 coast of the UK (Vardy et al., 2008). Acquired using the 3D Chirp subbottom profiler (Bull
234 et al., 2005), the 30×30 m volume is characterized by a strong bedrock reflector overlain by a
235 much weaker seabed. The selected area provides an interesting imaging challenge as it con-
236 tains a Second World War bomb crater, visible as a distinct bedrock depression with steep
237 sides ($\geq 10^\circ$) and sharp breaks of slope. The weakness of the seabed and steepness of slopes
238 relative to aliasing limits will highlight any deficiencies in the frequency approximation.

239 Figures 4a and 4b show inline sections and Figures 4d and 4e time slices (14.1 ms
240 twt), extracted from the volume migrated using ProMAX and the frequency-approximated

241 code (using the same frequency bands as for the synthetic data set; Table 1). The vertical
242 sections demonstrate very similar structural reconstruction. Migrating each frequency band
243 to an appropriate maximum dip angle (18° , 15° , 12° , 10° , 8° , and 8° for the six bands used;
244 Table 1) has resulted in better preservation of the higher frequencies (blue boxes, Figure 4),
245 whilst maintaining minimal contamination of the weaker seabed by steeply dipping aliased
246 energy (red boxes, Figure 4). The time slices extracted at 14.1 ms twt also show very
247 similar reflector reconstruction; the northern and southern slopes being imaged well, but
248 the steeper ($> 10^\circ$) eastern and western sides not being effectively reconstructed. Similarly,
249 the better high-frequency preservation in the frequency-approximated result can be seen
250 with tighter, better resolved reflectors on the southern crater flank (blue boxes; Figures
251 4d and 4e). There also appears to be less contamination by aliased energy than in the
252 traditionally antialiased Kirchhoff volume, where there is significant smearing of energy
253 deeper into the subsurface (red boxes, Figures 4d and 4e).

DISCUSSION

254 Figures 2, 3, and 4 demonstrate that, for both synthetic and field data, the frequency-
255 approximated approach to Kirchhoff migration better preserves higher frequencies than a
256 standard antialiased Kirchhoff migration, whilst simultaneously minimizing aliased energy.
257 Using just six narrow-band traces, structures can be accurately imaged with only a minor
258 increase in run time over the most simple time domain migration. Table 2 compares the run
259 times for Kirchhoff prestack migrations on the synthetic and field data examples described
260 previously using our frequency-approximated approach and a simple operator-truncated
261 time-domain algorithm without anti-aliasing. This ensures that the comparison is purely
262 in the evaluation of the Kirchhoff integral (equation 4) and not due to any differences in

263 optimisation of the overall migration between our code and the ProMAX Kirchhoff algo-
264 rithm. In both cases, the run time of the frequency-approximated Kirchhoff algorithm is
265 slower than a simple time domain Kirchhoff migration by a factor of ≈ 2.3 .

266 The strength of a frequency-domain approach to Kirchhoff imaging is the controlled
267 decimation of the frequency domain. This allows the processor to optimize the efficiency
268 by using only the minimum required number of frequency bands, along with the additional
269 advantage of these being few enough in number for manual specification of the frequency-
270 dependent dip filtering limits of the Kirchhoff operator. However, this strength is also a
271 potential weakness, as it relies on the assumption that the central frequency is representa-
272 tive of all frequencies in the narrow-band trace. If this assumption breaks down, energy will
273 cease to be migrated correctly and the imaged volume will become incoherent with poor can-
274 cellation of noise and indistinct reconstruction of reflectors (particularly those with steeper
275 dips). As such, a great deal of care and thought is required to define suitable frequency
276 bands.

277 The representativeness of the central frequency can be quantified using the -90 -degree
278 phase shift. We propose that it is representative if the difference in phase shift ($\lambda/4$) between
279 the central frequency and the minimum or maximum frequency in the band is below the
280 constructive summation limit of the seismic data. For the Chirp data examples, the limit
281 for constructive summation is defined as the main peak to side-lobe distance (± 2.9 cm in
282 1500 m/s velocity field). Using phase shift bands 5.0 cm wide, the source bandwidth can be
283 subdivided into six frequency bands (Figure 5). If the source waveform is not known with
284 confidence, we find bandwidths of about 0.5 octaves provides appropriate reconstruction of
285 the reflected wavelet (Figure 6).

286 Once the frequency bands are decided upon, creation of these narrow-band traces is
287 straightforward. With suitable tapering, simple band-pass filtering is adequate. Alter-
288 natively, swept frequency sources (such as Chirp or Vibroseis) are inherently frequency
289 decomposed. Since correlation with the source sweep combines acting as a band-pass filter
290 along with wavelet compression, correlation with a series of band limited sweeps will also
291 result in a set of narrow-band traces.

292 This technique has broader implications than increasing the efficiency of frequency do-
293 main Kirchhoff migration; applications might be found among Kirchhoff inversion algo-
294 rithms for example, particularly when performing time consuming and repetitive inversions
295 during velocity model construction. Additionally, as illustrated in Figure 7, frequency de-
296 composition into relatively few narrow bands affords the processor complete control over
297 the imaging of each frequency band. In locations and/or data sets where aliasing may be
298 a problem, this allows the frequency dependence of the Kirchhoff operator to be easily ma-
299 nipulated for optimal imaging, along with affording simple corrections for other frequency
300 dependent parameters, such as velocity dispersion and attenuation. Similarly, for swept fre-
301 quency applications in the marine environment, such as Chirp or Marine Vibroseis, where
302 the source location can change within the sweep length, frequency decomposition into a
303 series of narrow-band traces would allow this to be accommodated through separate posi-
304 tioning of each narrow-band trace.

CONCLUSION

305 Frequency-domain Kirchhoff migration offers significant advantages over a time-domain
306 approach, intrinsically accommodating antialias filtering. However, the need to frequency
307 decompose each input trace dramatically increases the required runtime. We have shown

308 that this frequency decomposition can be approximated by band-pass filtering into a few (six
309 for the example data shown) narrow-band traces with bandwidths determined from prior
310 knowledge of the source waveform. Kirchhoff migration of these traces using coefficients
311 determined at their central frequencies affords better preservation of the higher frequencies
312 and cancellation of aliased energy than traditional antialiased Kirchhoff algorithms. This
313 is achieved at an increase in computational expense over a simple time domain Kirchhoff
314 algorithm equivalent to pre- versus poststack imaging (≈ 2.3). For near-shore applications
315 this increase is small enough to permit near real-time application on a modern workstation.

ACKNOWLEDGMENTS

316 The authors wish to thank Richard Hobbs for the use of his Phase Screen 3D forward
317 modelling code, along with Justin Dix, Jonathan Bull, and Luke Pinson for their help in
318 acquiring the data used as the field data case study. We would also like to acknowledge
319 the contributions of John Bradford, Samuel Gray, Isabelle Lecomte, and an anonymous
320 reviewer. Their comments were extremely insightful, improving greatly the clarity and
321 overall quality of the manuscript. The standard prestack antialiased Kirchhoff migrations
322 were performed using Landmark's ProMAX software. All other processing used custom
323 algorithms.

REFERENCES

- 324 Abma, R., J. Sun, and N. Bernitsas, 1998, Anti-aliasing methods in Kirchhoff migration:
325 *Geophysics*, **64**, 1783–1792.
- 326 Bardan, V., 1987, Trace interpolation in seismic data processing: *Geophysical Prospecting*,
327 **35**, 343–389.
- 328 Baysal, E., D. D. Kosloff, and J. W. C. Sherwood, 1983, Reverse time migration: *Geo-*
329 *physics*, **48**, 1514–1524.
- 330 Berryhill, J. R., 1977, Diffraction response for nonzero separation of source and receiver:
331 *Geophysics*, **42**, 1158–1176.
- 332 Bevc, D. and J. Claerbout, 1992, Fast anti-aliased Kirchhoff migration and modelling:
333 Stanford Exploration Project, **Report 75**, 97–103.
- 334 Biondi, B., 2001, Kirchhoff imaging beyond aliasing: *Geophysics*, **66**, 654–666.
- 335 Bleistein, N., 1987, On the imaging of reflectors in the earth: *Geophysics*, **52**, 931–942.
- 336 ———, 1999, Hagedoorn told us how to do Kirchhoff migration and inversion: *The Leading*
337 *Edge*, **18**, 918–927.
- 338 ———, 2001, Mathematics of Multidimensional Seismic Imaging, Migration, and Inversion:
339 Springer-Verlag, Inc.
- 340 Bleistein, N. and S. H. Gray, 2001, From the Hagedoorn imaging technique to Kirchhoff
341 migration and inversion: *Geophysical Prospecting*, **49**, 629–643.
- 342 Buckingham, M., 2000, Wave propagation, stress relaxation, and grain-to-grain shearing in
343 saturated, unconsolidated marine sediments: *Journal of the Acoustics Society of America*,
344 **108**, 2796–2815.
- 345 Bull, J., M. Gutowski, J. Dix, T. Henstock, P. Hogarth, T. Leighton, and P. White, 2005,
346 Design of a 3D Chirp sub-bottom imaging system: *Marine Geophysical Researches*, **26**,

- 347 157–169.
- 348 Claerbout, J. and S. Doherty, 1972, Downward Continuation of Moveout-Corrected Seis-
349 mograms: *Geophysics*, **37**, 741–768.
- 350 Claerbout, J. F., 1992, Anti aliasing: Stanford Exploration Project, **73**.
- 351 Docherty, P., 1991, A brief comparison of some Kirchhoff integration formulas for migration
352 and inversion: *Geophysics*, **56**, 1164–1169.
- 353 Forgues, E., E. Scala, and R. G. Pratt, 1998, High resolution velocity model estimation
354 from refraction and reflection data: 68th Annual International Meeting, SEG, Expanded
355 Abstracts, 1211–1214.
- 356 Freudenreich, Y. and S. Singh, 2000, Full waveform inversion for seismic data-frequency
357 versus time domain: 62nd Annual Meeting, EAGE, Expanded Abstracts, C0054.
- 358 Gray, S., 1992, Frequency-selective design of the Kirchhoff migration operator: *Geophysical*
359 *Prospecting*, **40**, 565–572.
- 360 Gray, S. H., 1997, True-amplitude seismic migration: a comparison of three approaches:
361 *Geophysics*, **62**, 929–936.
- 362 Gutowski, M., J. M. Bull, J. Dix, T. Henstock, P. Hogarth, P. White, and T. Leighton, 2002,
363 Chirp sub-bottom profiler source signature design and field testing: *Marine Geophysical*
364 *Researches*, **23**, 481–492.
- 365 Hagedoorn, J. G., 1954, A process of seismic reflection interpretation: *Geophysical Prospect-*
366 *ing*, **2**, 85–127.
- 367 Hilterman, F. J., 1970, Three-dimensional seismic modeling: *Geophysics*, **35**, 1020–1037.
- 368 ———, 1975, Amplitudes of seismic waves – A quick look: *Geophysics*, **40**, 745–762.
- 369 Hubral, P., 1977, Time Migration – Some Ray Theoretical Aspects: *Geophysical Prospect-*
370 *ing*, **25**, 738–345.

- 371 Hubral, P., M. Tygel, and H. Zien, 1991, Three-dimensional true-amplitude zero-offset
372 migration: *Geophysics*, **56**, 18–26.
- 373 Lauo, Q. and G. A. McMechan, 1996, Multifrequency viscoacoustic modelling and inversion:
374 *Geophysics*, **61**, 1371–1378.
- 375 Lokshtanov, D., M. Denisov, and D. Finikov, 2002, Multiple suppression and datuming
376 with an antialias radon transform for marine 4C data: 64th Conference and Technical
377 Exhibition, EAGE, Extended Abstracts.
- 378 Lumley, D., J. Claerbout, and D. Bevc, 1994, Anti-aliased Kirchhoff 3-D migration: 64th
379 Annual International Meeting, SEG, Expanded Abstracts, 1282–1285.
- 380 Pratt, R. G. and M. H. Worthington, 1988, The application of diffraction tomography to
381 to cross-hole seismic data: *Geophysics*, **53**, 1284–1294.
- 382 Schleicher, J., M. Tygel, and P. Hubral, 2007, Seismic True-Amplitude Imaging, volume **12**
383 of Geophysical Developments Series: SEG.
- 384 Schneider, W. A., 1978, Integral formulation for the migration in two and three dimensions:
385 *Geophysics*, **43**, 49–76.
- 386 Sirgue, L. and R. G. Pratt, 2004, Efficient waveform inversion and imaging: A strategy for
387 selecting temporal frequencies: *Geophysics*, **69**, 231–248.
- 388 Troke, A. W., 1970, A simple theory for seismic diffractions: *Geophysics*, **35**, 762–784.
- 389 Vardy, M., J. Dix, T. Henstock, J. Bull, and M. Gutowski, 2008, Decimetre-resolution 3D
390 seismic volume in shallow water; A case study in small object detection: *Geophysics*, **73**,
391 B33–B40.
- 392 Whitmore, N. D., 1983, Iterative depth migration by backward time propagation: 53rd
393 Annual International Meeting, SEG, Expanded Abstracts, 382–385.
- 394 Wild, A. J. and J. A. Hudson, 1998, A geometrical approach to the elastic complex screen:

- 395 Journal of Geophysical Research, **103**, 707–725.
- 396 Yilmaz, O., 1987, Seismic Data Processing, volume **2** of Investigations in Geophysics: SEG,
- 397 1st edition edition.

Band	Freq. Limits (Hz)	$\Delta\omega$ (Hz)	ω_c (Hz)
1	1000-1400-1400-1800	400	1400
2	1400-1800-1800-2250	425	1800
3	1800-2250-2250-2750	475	2250
4	2250-2750-3500-4000	1250	3125
5	3500-4000-7000-8000	3450	5500
6	7000-8000-12000-13000	5000	10000

Table 1: Bands used during frequency-approximated Kirchhoff migration of data examples presented. Decomposition into narrow-band traces was performed using a zero phase Ormsby bandpass filter with 25% zero padding. Bandwidth $\Delta\omega$ is calculated using -3 dB (50% power) levels.

Volume	Freq. Approx.	Time Domain
	Kirchhoff	Kirchhoff
Synthetic Data	0 hr 19 min	0 hr 8 min
Field Data	0 hr 51 min	0 hr 23 min

Table 2: Summary of run times (performed on an off-the-shelf dual quad core workstation) for migrating synthetic and field data examples using the frequency-approximated Kirchhoff approach and an equivalent non-antialiased prestack Kirchhoff migration using the ProMAX algorithm.

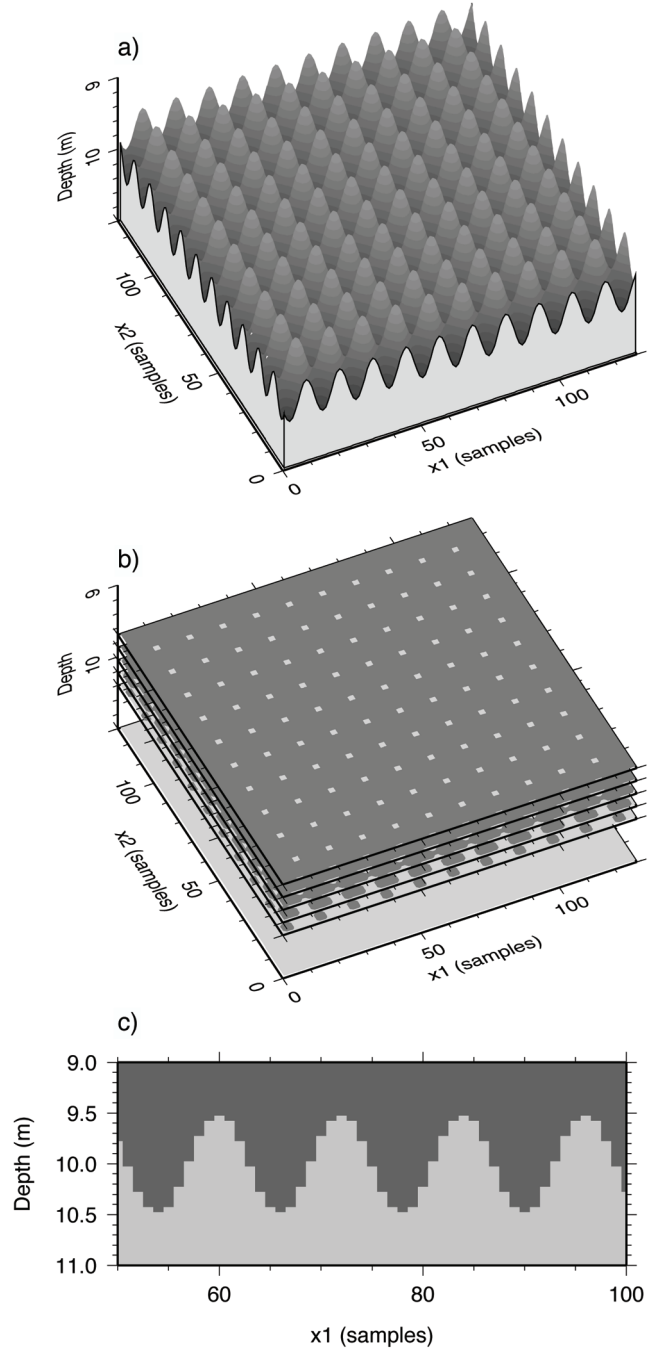


Figure 1: Map of sinusoid used to generate the step function interface between media, panel a), together with horizontally sliced screens, panel b), and vertical section, panel c), through the velocity model. Dark gray material has velocity and density of 1480 m/s and 1020 g/m³, while pale gray 1550 m/s and 1680 g/m³, respectively.

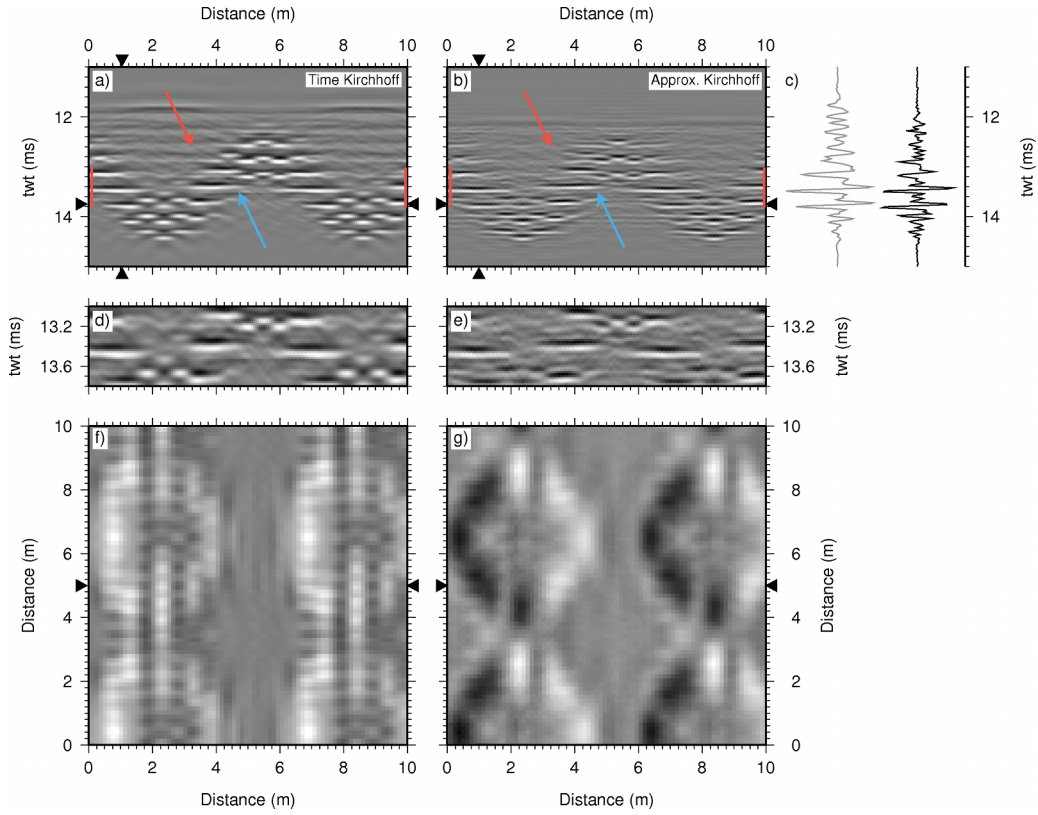


Figure 2: Imaged crossline sections through ProMAX, a) , and frequency-approximated, b), migrated volumes, together with time slices, f) and g), at 13.78 ms twt. Wiggle traces, c), compare trace extracted 1.0 m into section from ProMAX Kirchhoff (gray line) and frequency-approximated Kirchhoff (black line), while panels d) and e) show vertically exaggerated display of crosslines between 13.0 ms twt and 13.8 ms twt (red bars, panels a) and b)). Red arrows indicate anomalous reflectors and blue arrows energy smearing, respectively.

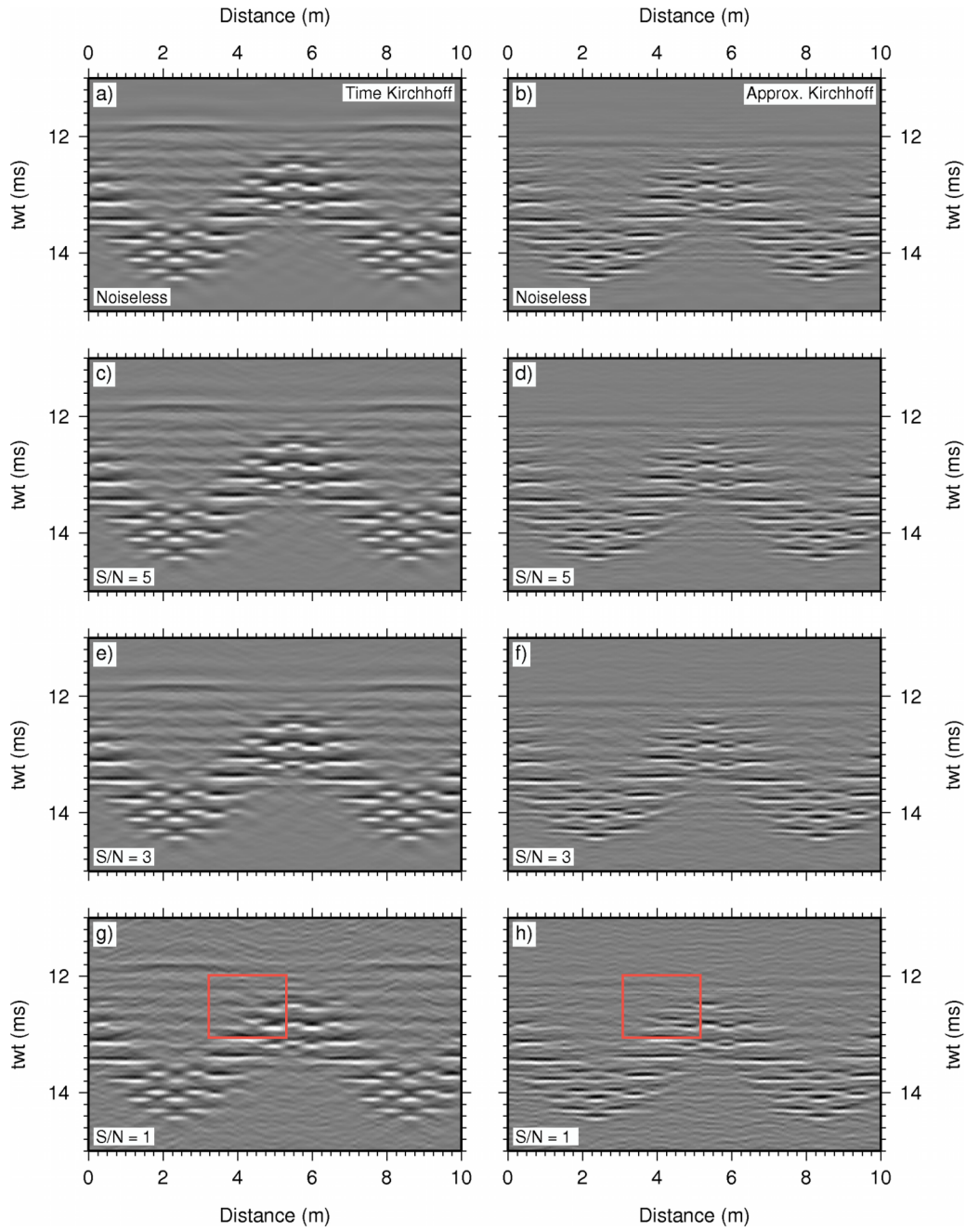


Figure 3: Eight panels showing results of sensitivity analysis on synthetic crossline shown in Figure 2. Panels a) and b) are noise-free baseline, while panels c) through h) show the effect of increasing noise on the imaged section, highlighted by black boxes in panels g) and h.).

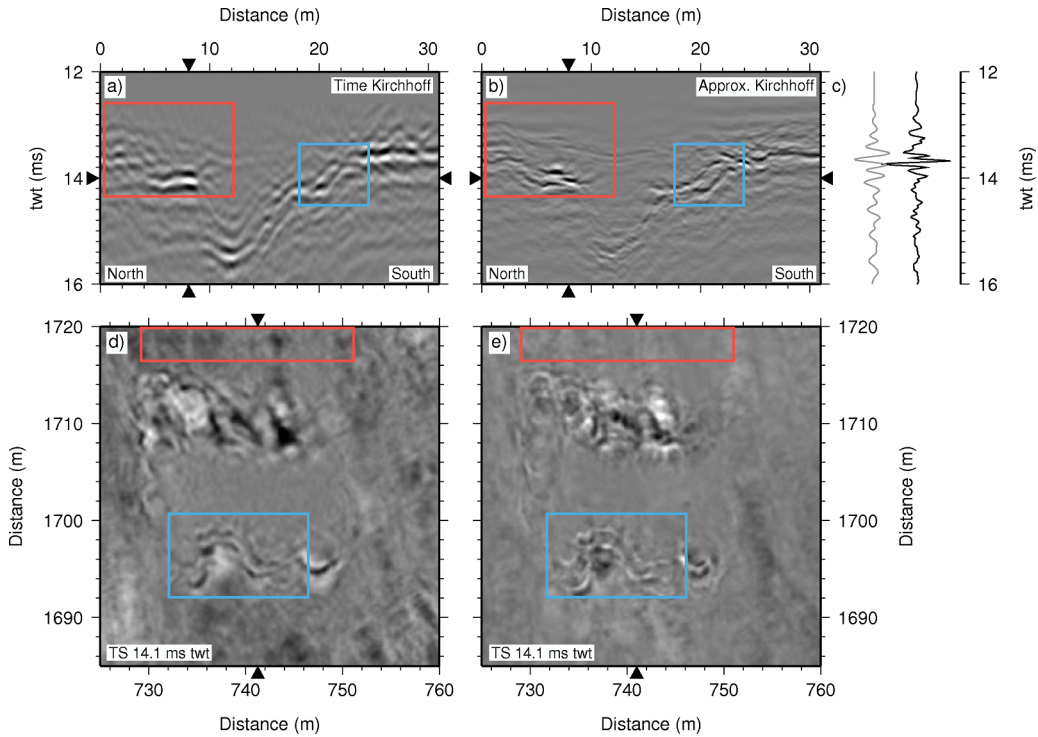


Figure 4: Imaged crossline sections through ProMAX, a), and frequency-approximated, b), migrated volumes, together with time slices, d) and e), at 14.10 ms twt. Wiggle traces, c), compare trace extracted 8.0 m into section from ProMAX Kirchhoff (gray line) and frequency-approximated Kirchhoff (black line). Red and blue boxes highlight aliased energy and frequency preservation, respectively.

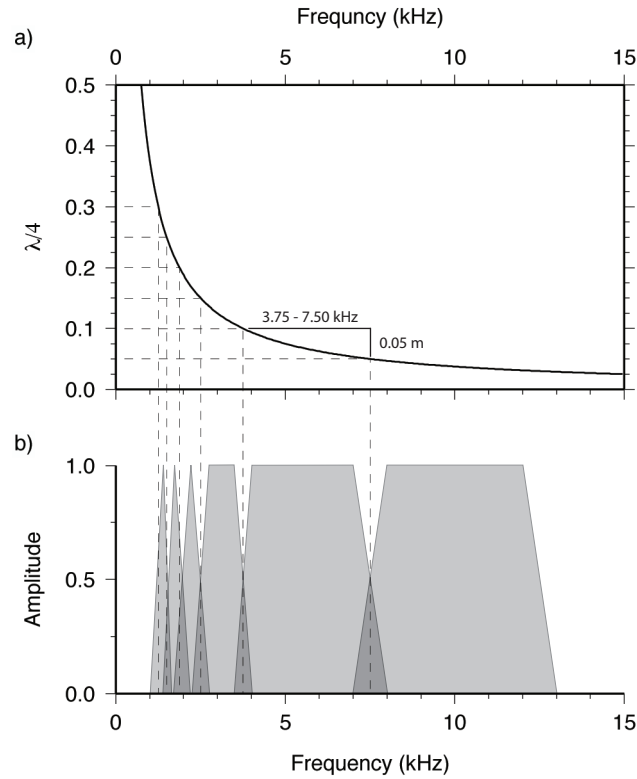


Figure 5: Illustration of relationship between phase shift ($\lambda/4$) and frequency bands. Panel a) shows how dividing the phase shift domain into 5.0 cm bands decimates the source bandwidth into a series of frequency bands. These can be used to define the set of bandpass filters in b).

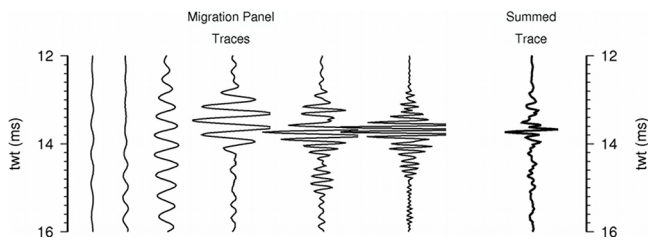


Figure 6: Bedrock reflection wavelets for each frequency band extracted 8.0 m into field data example. Amplitudes are scaled appropriately for contribution to final combined trace (thicker black).

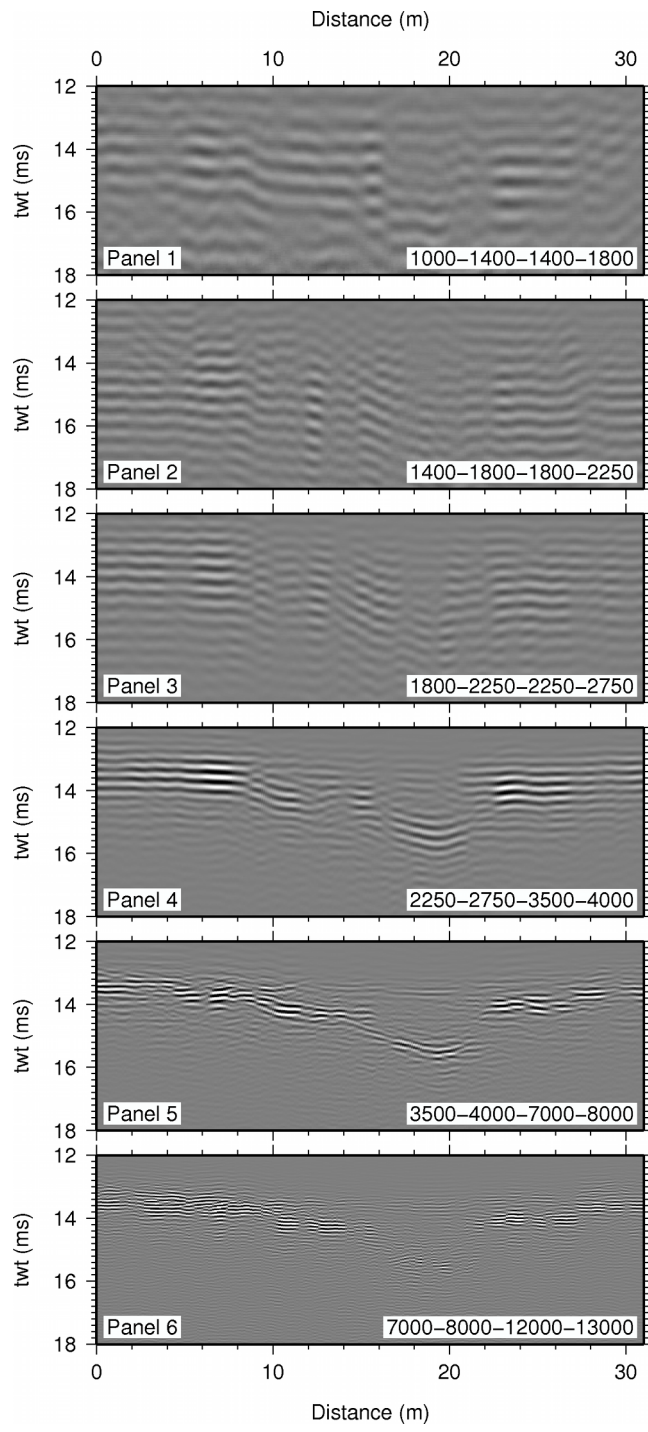


Figure 7: Six migration panels obtained using frequency bands defined in Figure 5 for field data inline section shown in Figure 4b.